Chapter 1
ZnS and ZnO Semiconductor Nanoparticles Doped with Mn^{2+} Ions. Size Effects Investigated by EPR Spectroscopy

M. Stefan, S.V. Nistor and D. Ghica

Abstract Electron paramagnetic resonance (EPR) spectroscopy has been extensively employed to investigate the presence, localization, distribution and interaction with the host crystalline lattice of the paramagnetic point defects (intrinsic defects and transition metal ions) in semiconductors. The retrieval of such information for nanostructured semiconductors is considerably more difficult, due to the high disorder level in such systems, reflected in broad, featureless EPR spectra. We show here how, with proper adjustments of the EPR experiments and accurate numerical analysis of the resulting spectra, it was possible to obtain more accurate information regarding the localization and structure of various Mn^{2+} centers in ZnS and ZnO semiconductor nanoparticles (NPs). This lead to the observation and investigation of size related effects such as the presence of the extended lattice defect assisted incorporation of impurities in small ($\sim$3 nm) cubic ZnS NPs, the dominant size induced lattice disorder observed for ZnO NPs, independent of the synthesis procedures, or the three steps decomposition of the ε-$Zn(OH)_2$ disordered shell of ZnS NPs with formation of new oxy-hydrated zinc compounds. These effects can be used to synthesize semiconductor nanoparticles with controlled size distribution, doping level and functionalized surfaces for specific technological applications.

1.1 Introduction

Small size (d < 10 nm) II–VI semiconductor nanoparticles (NPs) doped with transition metal ions (TMIs) have been intensely investigated during the last two decades in search for superior or even new optical, electrical and magnetic prop-

M. Stefan (✉) · S.V. Nistor · D. Ghica
National Institute of Materials Physics, 077125 Bucharest, Magurele, Romania
e-mail: mstefan@infim.ro

S.V. Nistor
e-mail: snistor@infim.ro

D. Ghica
e-mail: ghica@infim.ro

V. Kuncser and L. Miu (eds.), *Size Effects in Nanostructures*,
Springer Series in Materials Science 205, DOI 10.1007/978-3-662-44479-5_1

erties, associated with the reduced size, for a wide range of technological applications [1–3]. One of the envisaged goals has been to use size effects to tailor the material properties. The main size related factors affecting the semiconductor NP properties are the quantum confinement and the large surface to volume ratio which could lead to the dominance of surface over the core effects in the physico-chemical properties. For very small NPs (<3 nm), where more than 30 % of atoms are in the surface layer, the surface states can strongly influence the core structural properties as well [4, 5].

Doping with well-chosen impurities is one of the most widely used techniques to alter the electric and optical properties of a bulk semiconductor. During the last decade doping with activation ions has been explored extensively as a technique to further modify the properties of semiconductor nanoparticles [6, 7]. The largest part of the research efforts was focused on wide band-gap ZnS and ZnO semiconductor NPs doped with TMIs, due to their exceptional intrinsic physical properties [3, 8–10] and their singular non-toxic character between the II–VI compounds, of special interest in bio-medical applications [11, 12].

One of the most investigated activating ions is Mn^{2+}, whose presence in the host semiconductors gives rise to exceptional optical and magnetic properties [8, 9, 13]. Doping II–VI nanostructured semiconductors with Mn^{2+} ions leads to high fluorescence efficiency and magnetic ordering, with potential applications for luminescent and spintronic devices, respectively [3, 14, 15]. Moreover, large concentrations of Mn^{2+} ions incorporated at substitutional sites can modify the lattice parameters as well as the band gap of semiconducting nanomaterials.

The efficient tailoring of the doped nanostructured semiconductor properties for various applications cannot be achieved without accurate knowledge of the localization, concentration and electronic state properties of the doping Mn^{2+} ions. The method of choice for obtaining such information is the electron paramagnetic resonance (EPR)/electron spin resonance (ESR) spectroscopy [16, 17]. EPR has played a key role in the study of point defects in bulk semiconductors for more than sixty years, as the most powerful tool for defect identification and atomic structure determination. EPR data can complement the information gained by other structural methods, being able for instance to provide information about the presence of minute amounts of different phases/compounds, which are below the $\sim$2 % detection limit of X-ray diffraction (XRD) and/or have a highly disordered structure and can be observed but not identified by transmission electron microscopy (TEM).

In the particular case of semiconductor nanoparticles, EPR spectroscopy can offer accurate information concerning the localization of the activating TMIs in the volume and on the surface of the nanoparticles, the configuration of their neighboring ligands and the local structural/bonding modifications induced by external excitations (temperature, radiation). It should be noted that the Mn^{2+} ions are particularly suitable as sensitive atomic probes in Zn based compounds, as they have similar charge state and very close ionic radius with the host Zn^{2+} cations [18]. They can also be employed as EPR probes with low perturbing effects to observe the fine changes in the structure and composition of (nano)crystalline II–VI compounds induced by various thermo-chemical treatments [19–24].

This chapter is focused on the use of EPR to investigate nanostructured ZnS and ZnO doped with low levels of Mn^{2+} ions, with emphasis on the observed size related characteristics and properties. The low concentration of these paramagnetic ions is important for a better resolution of the spectra, allowing more information to be extracted. The results presented here largely reflect the progress made in the last few years in our research group from the Center for advanced ESR techniques (CetRESav: cetresav.infim.ro) in developing methods and software for the accurate analysis of the EPR spectra of Mn^{2+} ions in (nano)crystalline materials with various degrees of disorder and their use in investigating the local structure of nanosized ZnS and ZnO. The discourse is structured in two parts, underlying the use of the developed EPR methods and software for the characterization of defect centers and for extracting information about the NPs host lattice itself. Thus, in the first part the determination of the localization of the Mn^{2+} ions in small colloidal ZnS and ZnO NPs is discussed, with special attention paid to the technique used to overcome the problems associated with the size and disorder of these nanosystems. The second part presents examples of EPR probing of chemical/structural transformations in nanostructured semiconductors, such as the preparation of ZnO NPs by thermal decomposition of Zn based compounds and the crystallization of the resulting nanostructured ZnO.

1.2 EPR Spectroscopy of Mn^{2+} Ions in (Nano)Crystalline ZnS and ZnO

EPR consists in the resonant absorption of microwave photons in a sample containing paramagnetic centers/defect centers with unpaired electrons submitted to a static magnetic field **B**. An example of paramagnetic centers are the TMIs of interest, which have unpaired electrons in the inner partially filled shell, giving rise to a non-zero electron spin angular momentum **S** and an associated magnetic moment **μ**, given by:

$$\boldsymbol{\mu} = -\mathbf{g}\beta\mathbf{S} \tag{1.1}$$

Here **g** is the gyromagnetic or g-factor and β the Bohr magneton. For weakly bound electrons g is close to the free electron value $g_e = 2.0023$ and nearly isotropic. The potential energy of the magnetic moment **μ** in the presence of an external magnetic field **B**, known as electron Zeeman energy, is described by:

$$E = -\boldsymbol{\mu} \cdot \mathbf{B} = \beta\mathbf{B} \cdot \mathbf{g} \cdot \mathbf{S} \tag{1.2}$$

In order to illustrate the principle of the magnetic resonance spectroscopy, let us consider the simple case of a free electron ($S = 1/2$). In the presence of a magnetic field the free electron has two energy levels, corresponding to the two magnetic quantum numbers $M_S = \pm 1/2$:

$$E_{\pm} = \pm\frac{1}{2}\beta g B \tag{1.3}$$

In a typical EPR experiment, the microwave absorption spectrum is obtained by sweeping the external magnetic field at a fixed microwave frequency, rather than sweeping the frequency. Commercially available EPR spectrometers are built for microwave frequencies of 9.4–9.8 GHz (X-band), 34 GHz (Q-band) and 94 GHz (W-band). For a fixed frequency v_0 the EPR transition occurs at the magnetic field value B_0 where the resonance condition $E_+ - E_- = hv = \beta g B_0$ is fulfilled, h representing the Planck constant.

The interpretation of the EPR spectra is done using the spin-Hamiltonian (SH) formalism. The EPR study of a paramagnetic center involves measuring microwave ($\sim$1–10 cm^{-1}) transitions within a small group of states which lies typically $\sim 10^3$–10^4 cm^{-1} below all others. In a formal way, these ground state levels can be regarded as an isolated set whose properties may be described without reference to the other levels. We associate an effective spin S_{eff} to the ground state manifold, resulted from considering the number of levels in the ground manifold as $(2S_{eff} + 1)$. The SH is the Hamiltonian operator of the effective spin and, as we show further, it describes the effect of the external magnetic field, hyperfine (hf) and crystal field interactions on the ground state levels of the paramagnetic centers [16, 17]. The diagonalization of the Hamiltonian matrix yields the eigenvalues and eigenstates of the ground manifold under all interactions present. The EPR transitions, responsible for the resonance lines in the microwave spectrum, can be derived from the obtained eigenvalues. When only the electron Zeeman interaction is present, the SH is simply:

$$\mathbf{H} = \beta \mathbf{B} \cdot \mathbf{g} \cdot \mathbf{S} \tag{1.4}$$

which splits the ground level into $2S + 1$ energy levels described by the magnetic quantum numbers $M_S = \pm S, \pm (S - 1) \ldots$.

In the case of TMIs containing nuclear isotopes with non-zero nuclear spin I, the interaction between the associated hyperfine magnetic field with the unpaired electron magnetic moment is described by an additional so-called hf term $\mathbf{S} \cdot \mathbf{A} \cdot \mathbf{I}$ in the spin Hamiltonian, where $\mathbf{A}$ is the hf interaction/coupling parameter. Thus, the resulting SH takes the form:

$$\mathbf{H} = \beta \mathbf{B} \cdot \mathbf{g} \cdot \mathbf{S} + \mathbf{S} \cdot \mathbf{A} \cdot \mathbf{I} \tag{1.5}$$

The hf interaction splits each electron level in $2I + 1$ sublevels corresponding to the quantum numbers $M_I = \pm I, \pm (I - 1) \ldots$ Its presence is observed in the EPR spectra as a hf structure, which is illustrated in Fig. 1.1 for the case of a $S = I = 1/2$ spin system. As depicted in Fig. 1.1b, the EPR transitions occur between levels with the same M_I, according to the selection rule for allowed magnetic dipole transitions: $\Delta M_S = \pm 1, \Delta M_I = 0$, when the splitting of the energy levels in the magnetic field $\mathbf{B}$ matches the fixed energy of the microwave quanta hv_0. The EPR lines

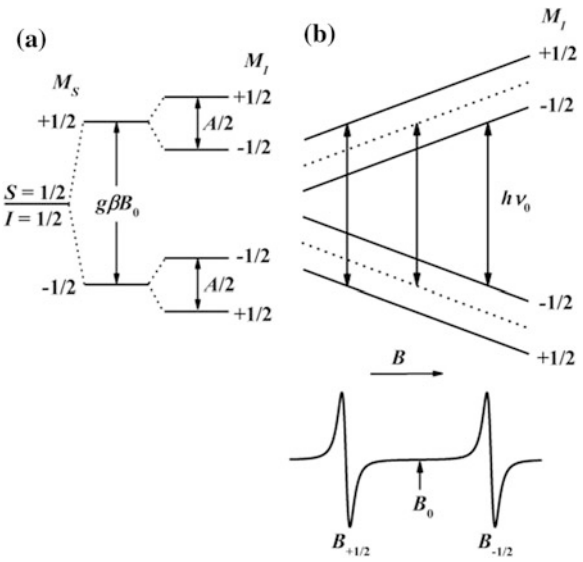

Fig. 1.1 **a** The energy levels structure of a paramagnetic center with $S = I = 1/2$ and **b** the allowed EPR transitions (*top*) and the corresponding EPR spectrum (*bottom*) for the same center when the magnetic field B is increased at fixed microwave frequency ν_0

corresponding to the allowed transitions are represented below, as derivatives of the absorption lines, which is the most common way to record an EPR signal.

One should also include in the SH the nuclear Zeeman interaction term $-\beta_N g_N B \cdot I$ due to the interaction between the nuclear magnetic moment and the external magnetic field, where β_N is the nuclear magneton and g_N is the nuclear g-factor, a constant depending on the type of nucleus. However, quite often this interaction is neglected because of its small value compared with the other interaction terms in the SH.

The dopant TMIs localized in the crystal lattice host are subjected to an electric local crystal field produced by the surrounding lattice ions, mainly by the first shell of neighboring ions. The local crystal field influences the TMIs through the spin-orbit interaction related with the presence of an electron orbital magnetic moment as well. In the absence of any neighboring charge compensating defect, the local point symmetry properties at the substitutional impurity TMI are usually those corresponding to the substituted lattice ion. They are reflected in the symmetry properties of the EPR spectra recorded when the host single crystal sample is rotated in the external magnetic field.

The intensity and symmetry of the local crystal field and the nature of the neighboring lattice ions are reflected in the interaction parameters of the SH. Thus, for non-cubic crystal fields both **g**- and **A**- parameters can be anisotropic, being described by (pseudo)tensors [16, 17]. Moreover, for electron spin values $S \geq 1$, the interaction with the crystal field is described by adding new terms in the SH, called zero field splitting (*ZFS*) terms, according to the local symmetry.

This interaction will be further illustrated in the case of the Mn^{2+} ions with a ^6S ($3d^5$) ground electron state, electronic spin $S = 5/2$ and nuclear spin $I = 5/2$ from the 100 % abundant ^{55}Mn isotopes. The SH for these ions can be written as [25]:

$$\mathbf{H} = \beta \mathbf{B} \cdot \mathbf{g} \cdot \mathbf{S} + \mathbf{S} \cdot \mathbf{A} \cdot \mathbf{I} + \mathbf{H}_{ZFS} - \beta_N g_N \mathbf{B} \cdot \mathbf{I} \tag{1.6}$$

The *ZFS* term $\mathbf{H}_{ZFS}$ is a sum of the Stevens operators, reflecting the local symmetry at the paramagnetic ion,

$$\mathbf{H}_{ZFS} = B_2^0 \mathbf{O}_2^0 + B_2^2 \mathbf{O}_2^2 + B_4^0 \mathbf{O}_4^0 + B_4^m \mathbf{O}_4^{\mathrm{m}} \tag{1.7}$$

where $m = 1, 2, 3, 4$ [16, 26]. For a cubic local symmetry $B_2^0 = B_2^2 = 0$ and $m = 4$, with $B_4^4 = 5B_4^0$. For axial symmetry $B_2^2 = 0$ and the m value specifies whether the symmetry axis is tetragonal ($m = 4$) or trigonal ($m = 3$), while for rhombic or lower symmetry all *ZFS* parameters could be non-zero.

The ^{6}S ground electron state of the Mn^{2+} ion, which is weakly interacting with the lattice host, leads to well resolved EPR spectra, with narrow lines over a broad temperature range, with a characteristic hyperfine structure of $2I + 1 = 6$ component lines. The interaction with the crystal field determines further splitting of the energy levels leading to a fine structure of $2S = 5$ components. Considering a single crystal (SC) sample doped with Mn^{2+} ions, the EPR spectrum for a particular orientation of the static magnetic field with respect to the sample would consist of $2S(2I + 1) = 30$ lines attributed to the allowed $\Delta M_S = \pm 1, \Delta M_I = 0$ transitions, whose positions vary with the orientation of the magnetic field. As an example, the EPR spectrum of the Mn^{2+} ions in a cubic ZnS (cZnS) single crystal with high crystal lattice perfection, doped with 500 ppm Mn [27], is shown in Fig. 1.2a (top). The spectrum,

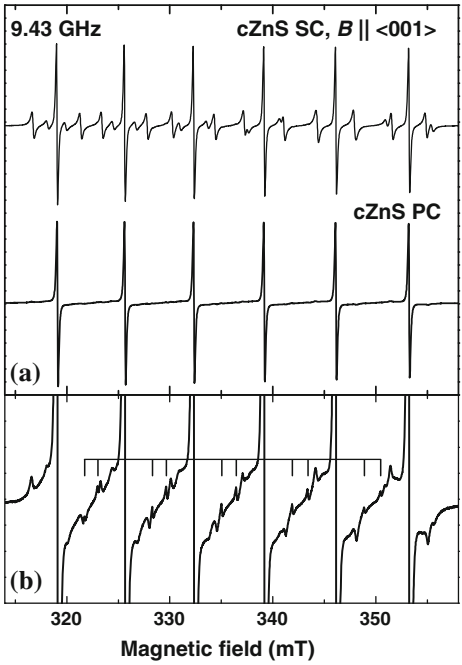

Fig. 1.2 **a** X-band EPR spectra of the Mn^{2+} ions in cZnS. *Top*: single crystal (SC) spectrum measured along the ⟨001⟩ crystalline axis. *Bottom*: spectrum of a polycrystalline (PC) sample. **b** Detailed view of the non-central transitions of the Mn^{2+} spectrum in the cZnS PC sample recorded at higher gain. The positions of the forbidden transitions are marked with *vertical lines*

Table 1.1 The SH parameters (*g, A, ZFS*) of the paramagnetic centers attributed to Mn^{2+} ions in ZnS with various structures and Zn based compounds

Lattice host/ center	*g*	*A* (10^{-4} cm^{-1})	*ZFS* (10^{-4} cm^{-1})	ΔB_{pp} (mT)/$\sigma(B_n^m)$ (% B_n^m)	Reference
cZnS single crystal/substitutional Mn^{2+}	2.00225	−63.88	$B_4^0 = -0.0444$ $B_4^3 = -1.2558$	0.097 (X)	[27]
cZnS NPs/ Mn^{2+}(I)	2.0022	−63.70	$B_2^0 = -13.7$ $B_4^0 = -0.0411$ $B_4^3 = -1.1549$	0.31 (X), 0.34 (W)/43 %B_2^0, 50 %B_4^0, 50 %B_4^4	[25]
cZnS NPs/ Mn^{2+}(II)	2.0012	−80.5	$B_2^0 = 20$–30	0.4 (X, W)/63 %B_2^0 for $B_2^0 = 27 \times 10^{-4}$ cm^{-1}	[25]
cZnS NPs/ Mn^{2+}(III)	2.0009	−86.8	$B_2^0 = 25$–35	1.1 (X, W)/ 53 %B_2^0 for $B_2^0 = 30 \times 10^{-4}$ cm^{-1}	[25]
Mixed polytype ZnS crystal/trigonal PN	2.0018	−64.9	$B_2^0 = 12.03$ $B_4^0 = -0.0411$ $B_4^3 = -1.1549$		[36]
Crystalline ε-$Zn(OH)_2$/substitutional Mn^{2+}	2.0010	−87.0	$B_2^0 = 23$–200	0.8 (Q)/41 %B_2^0 for $B_2^0 = 70 \times 10^{-4}$ cm^{-1}	[22]

The individual linewidth (ΔB_{pp}) for a specific microwave frequency band and the broadening parameter $\sigma(B_n^m)$ are also given

consisting of the 30 allowed transitions, was measured along the ⟨001⟩ crystalline axis, for which the hyperfine and fine structure are best resolved. By measuring the variation of the EPR spectra in three mutually perpendicular planes, one can accurately determine the SH parameters. From these parameters a wealth of information about the Mn^{2+} centers, such as the local symmetry, structure and type of ligands can be obtained. In the case of the Mn^{2+} impurity ions in the cZnS single crystals the symmetry properties of the spectrum and the resulting SH parameters (Table 1.1) showed that the Mn^{2+} ions substituted for the Zn^{2+} ions in nodes with cubic T_d symmetry [27].

If the measured sample is in a powder form, the information that can be obtained from the EPR spectrum of the Mn^{2+} ions is considerably reduced due to the spatial averaging over all crystalline directions. In Fig. 1.2a the bottom EPR spectrum was recorded on a polycrystalline (PC) cubic ZnS sample consisting of micrometer sized crystallites, with a similar 500 ppm manganese doping level [25]. Due to the spatial averaging over all crystalline directions, only the six central hyperfine lines ($M_S : -1/2 \leftrightarrow +1/2$, $\Delta M_I = 0$) of the Mn^{2+} ions, which exhibit a very small anisotropy, are still visible. The non-central lines ($M_S : \pm 1/2 \leftrightarrow \pm 3/2$, $\pm 3/2 \leftrightarrow \pm 5/2$, $\Delta M_I = 0$) can barely be distinguished from the noise level, due to line broadening induced by both higher anisotropy and lattice strains. Figure 1.2b depicts a spectrum recorded on the same polycrystalline sample, at very high gain, where the fine structure becomes visible.

It should be mentioned that for large enough *ZFS* parameters, especially in non-cubic crystal fields, the so called hyperfine forbidden transitions, determined by the selection rules $\Delta M_S = \pm 1, \Delta M_I = \pm 1$, with a considerably lower intensity I_f compared to the intensity I_a of the allowed transitions, can be more easily observed in the EPR spectra. For the substitutional Mn^{2+} centers with cubic symmetry in the cZnS SC I_f is very small, cancelling completely along the $\langle 001 \rangle$ crystalline axis [27]. However, as the positions of the ten central forbidden hyperfine transitions ($M_S : -1/2 \leftrightarrow +1/2$, $\Delta M_I = \pm 1$) are highly isotropic, their summed intensities in the cZnS PC spectrum are comparable with the intensities of the non-central allowed transitions (Fig. 1.2b).

In nanocrystalline powders the EPR spectra of the Mn^{2+} ions are further complicated by the increased lattice disorder induced by the surface [4] and wider size distribution, which results in large fluctuations of the local crystal fields, reflected in broader lines and associated loss of resolution. Moreover, there are often contributions from several Mn^{2+} centers with partially overlapping lines, due to the localization of the Mn^{2+} ions at various sites, in the core and on the surface of the nanoparticles. For such systems the determination of the SH parameters becomes even more difficult. An example is the case of Mn^{2+} doped cZnS NPs, one of the most EPR investigated II–VI nano-semiconductor, for which a rather large number of paramagnetic centers attributed to isolated Mn^{2+} ions with different SH parameter values and local symmetry were reported in the 1995–2006 decade (see the review of Bhattacharyya et al. [18]). As discussed in [25], especially for the Mn^{2+} ions substituting the Zn^{2+} cations, it is very likely that in many cases we are not dealing with actually different centers, but with different SH parameters reported for the same centers. Such a situation could result from a lower accuracy in the determination of the SH parameters, due to both too low resolution of the investigated EPR spectra and not sufficiently accurate analysis.

In order to overcome these problems we have developed an accurate analysis procedure based on the lineshape simulation and fitting of the multifrequency EPR spectra [25]. The advantage of measuring the EPR spectra of a sample at two different frequencies is that (1) it is possible to better separate the lines from various paramagnetic centers and (2) the effect of the different SH terms on the EPR transitions position and intensity varies with the measuring frequency.

Figure 1.3 displays the higher resolution EPR spectra of Mn^{2+} centers in a powder sample of cZnS nanoparticles self-assembled into a mesoporous structure [28] measured in two microwave frequency bands, namely W (top) and X (bottom). The spectra are attributed to two centers called Mn^{2+}(I) and Mn^{2+}(III), the first one consisting of substitutional Mn^{2+} ions in the core of the cZnS NPs and the second one, sensitive to the thermal history of the sample, consisting of Mn^{2+} ions localized in the surface layer / shell of the nanoparticles [25, 29, 30]. One can see that at very high frequency, in the W-band, the lines of the two centers are much better separated, due to the relative shift of the gravity centers of their spectra. This allows a better resolution in the reading of their transition fields and, therefore, in the determination of their SH parameters.

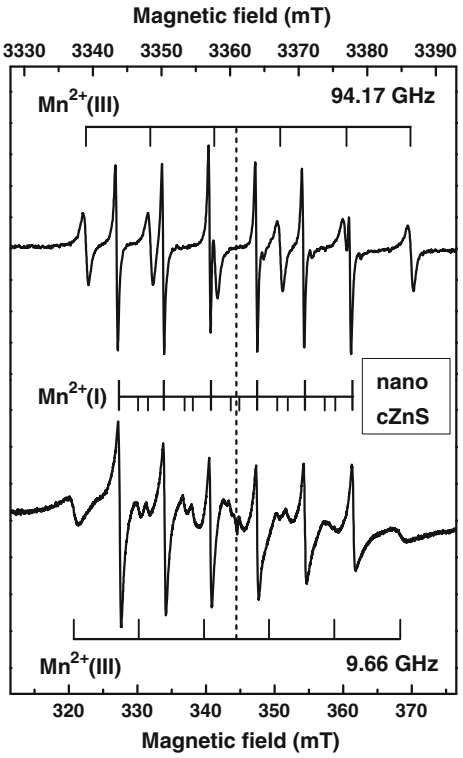

Fig. 1.3 High (W-band) and low (X-band) frequency EPR spectra of the Mn^{2+} ions in cZnS nanoparticles. The *dot line* marks the center of the Mn^{2+}(I) spectrum

Unlike the EPR spectrum of the Mn^{2+} ions in polycrystalline and single crystal cZnS, the intensity of the ten central forbidden hyperfine transitions in the low frequency EPR spectrum of the substitutional Mn^{2+}(I) centers in cZnS nanoparticles is significant (Fig. 1.3, bottom spectrum). As will be further shown, the presence of these transitions indicates a lowering of the local symmetry at the Mn^{2+} ions from cubic to at least axial, modeled by the addition of second order contributions to the *ZFS* term in the SH [29]. One can see that in the high frequency spectrum (Fig. 1.3, top spectrum) the forbidden hyperfine transitions of the Mn^{2+}(I) centers are not visible anymore, due to the fact that the relative intensity of the forbidden transitions with respect to the allowed transitions I_f/I_a is proportional to $\left(B_2^0/g\beta B\right)^2$ [16]. The positions of the allowed and forbidden transitions are also influenced by the axial *ZFS* term in the second $[\sim (B_2^0)^2/(g\beta B)]$ and third $[\sim A(B_2^0)^2/(g\beta B)^2,\ \sim A^2 B_2^0/(g\beta B)^2]$ approximations, according to the perturbation theory, thus affecting the relative intensities of the powder lines [25]. This frequency / field dependence of the transition intensities and positions shows that most information about the *ZFS* parameters can be retrieved from the low frequency spectra, where their influence is the strongest. On the other hand, when $B_2^0 \ll g\beta B$ (e.g. $B_2^0 < 20 \times 10^{-4}$ cm^{-1} for 94 GHz), the high frequency

spectra allow a very accurate determination of the g and A parameters, which for Mn^{2+} in the bulk II–VI semiconductors are isotropic [31].

An important feature of the EPR spectra of Mn^{2+} in small NPs is the strong line broadening which practically wipes out the non-central allowed transitions. The broadening effects are due to the presence of random strains, electrical fields and other perturbations from the extended lattice defects in the crystal lattice, resulting in a variation in the local crystal field at the paramagnetic ions, both in magnitude and orientation. The line broadening is reproduced in the lineshape simulation of the experimental spectra by including Gaussian distributions of the *ZFS* parameter B_n^m values, the broadening parameters being represented by the standard deviations of the *ZFS* parameter values $\sigma(B_n^m)$. In order to facilitate data comparison, $\sigma(B_n^m)$ values are further given as percentage of the corresponding B_n^m values.

When performing a lineshape simulation, besides the EPR parameters, the peak-to-peak linewidth ΔB_{pp} in the absence of the strain induced broadening effects is also specified. The EPR linewidth is due to the finite life-time of the spin states, which is determined by the dissipation of energy via the thermal vibrations of the lattice (spin-lattice relaxation), and to magnetic dipolar and exchange interactions between the paramagnetic centers present in the sample (spin-spin relaxation). Unresolved hf structures from the interaction with the nuclei of the neighboring ions can also contribute to the anisotropic line broadening. EPR spectra with narrower lines and, consequently, with better resolution, can thus be obtained for lower dopant concentrations and at lower measuring temperatures, where the spin-lattice relaxation time increases.

1.2.1 Multifrequency Lineshape Simulation Procedure for the Determination of the Mn^{2+} SH Parameters in Nanocrystals

As stated in the previous section, we have developed a two steps analysis procedure for the accurate determination of the SH parameters of the EPR spectra of Mn^{2+} ions in nanocrystalline materials. The procedure [25] requires EPR spectra recorded at both low and high microwave frequencies, usually in the X- and Q/W-bands, respectively. It is based on the lineshape simulation and fitting of the EPR spectra, including the hyperfine forbidden transitions and line broadening effects. In the first step one determines the g- and hf A- parameters from the high frequency spectrum. In the second step, with these two parameters fixed, one determines the *ZFS* parameters by lineshape simulation and fitting of the low frequency spectrum, as described in [25]. We employed for the lineshape simulations the EasySpin v. 4.0 software [32], which we extended for very large broadening parameters with the weighted summation procedure outlined in [33].

The multifrequency analysis procedure presented above was first employed for the accurate determination of the SH parameter values of the Mn^{2+} centers in cZnS nanoparticles self-assembled in a mesoporous structure, exhibiting very narrow EPR lines, of 0.4 mT at room temperature (RT), the smallest value reported until then for these systems [28, 29]. In the following sections this procedure will be employed for the analysis of the EPR spectra of Mn^{2+} in two samples consisting of newly prepared colloidal cZnS and ZnO nanoparticles, respectively, doped with low concentrations of Mn^{2+} ions in order to diminish the line broadening induced by magnetic dipolar interactions.

1.2.2 Localization of the Mn^{2+} Ions in Colloidal cZnS Nanoparticles

The investigated cZnS nanocrystalline sample was synthesized by co-precipitation in a surfactant-assisted liquid-liquid reaction, following the procedures reported in [28, 34]. Thus, 0.1 % mol manganese acetate [$Mn(CH_3–COO)_2 \cdot 4H_2O$] was added to the solution of zinc acetate [$Zn(CH_3COO)_2 \cdot 2H_2O$], being further mixed for 15 min and afterwards co-precipitated with sodium sulfide [$Na_2S \cdot 9H_2O$] in the presence of the Tween 20 surfactant, at optimum pH = 8. The reaction took place under argon gas to diminish any unwanted reaction with the atmospheric oxygen and carbon dioxide. In the post synthesis steps the precipitate was filtered, washed with bi-distilled water and methanol, and dried at 50 ºC for 24 h. The resulting powder consisted of cZnS nanoparticles, self-assembled in a mesoporous structure. The X-ray diffractogram of the ZnS nanoparticles sample is displayed in Fig. 1.4.

The restrictive effect of the self-assembling on the growth of the individual nanoparticles resulted in a tighter size distribution centered on 2 nm and improved nanoparticles crystal lattice quality, in agreement with the results of XRD

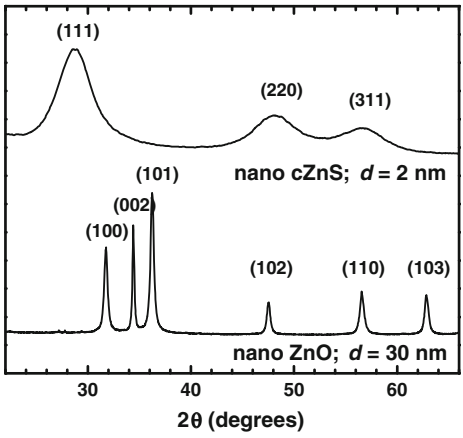

Fig. 1.4 X-ray diffractograms of the colloidal Mn^{2+} doped cZnS and ZnO nanoparticles

investigations which have shown that the surface induced degree of disorder decreases for aggregated nanocrystals [4]. This was reflected in derivative peak-to-peak linewidths of less than 0.4 mT for the X-band EPR lines. The EPR spectra of this sample, recorded at low and high frequency, are those displayed in Fig. 1.3.

In a lattice host with cubic symmetry the Mn^{2+} ions, with similar valence state and very close size to the host cations, would be expected to substitute the Zn^{2+} ions in tetrahedrally coordinated sites with cubic symmetry and give EPR spectra described by a SH containing only the fourth order (cubic) *ZFS* terms. Indeed, as shown in the previous section, in bulk cZnS single crystals only such Mn^{2+} centers with cubic symmetry could be observed [27]. However, a careful analysis of the EPR spectra of the substitutional Mn^{2+} centers in small cZnS NPs (the Mn^{2+}(I) centers) has shown that the Mn^{2+} ions are localized at sites with lower symmetry, reflected in the necessity to add second-order *ZFS* terms to the SH in order to describe the observed spectra [29]. As shown in [25], the only *ZFS* term found to exhibit a notable influence on the Mn^{2+} EPR spectrum in cZnS NPs is the B_2^0 axial term, which can be determined with the procedure outlined in the previous section.

The SH parameters of the two Mn^{2+} centers observed in the mesoporous cZnS sample, determined with this procedure, are given in Table 1.1. Figure 1.5 displays the experimental and simulated spectra at low and high frequency.

The SH parameters of the Mn^{2+}(I) centers are very close to those reported earlier for substitutional Mn^{2+} ions at trigonally distorted cation sites in highly defective cZnS single crystals (called PN centers) (see Table 1.1), distortion attributed to a neighboring stacking defect [35, 36]. This result leads to the conclusion that the Mn^{2+}(I) centers exhibit a similar structure with the PN centers, i.e. the Mn^{2+} ions are localized in the core of the cZnS NPs at Zn^{2+} cation sites situated next to an extended lattice defect, which is responsible for the local axial distortion of the otherwise cubic crystal field [29]. It should be mentioned that no trace of substitutional Mn^{2+} centers with cubic symmetry could be found in the recorded EPR spectra, showing that *the Mn^{2+} ions enter the cZnS NPs lattice only in the neighborhood of an extended defect*. Therefore, we proposed that the incorporation of the Mn^{2+} impurity ions in the very small cZnS NPs (quantum dots) prepared at low temperatures, by colloidal synthesis, took place by an extended lattice defects assisted (ELDA) mechanism [29, 37]. According to the ELDA mechanism of incorporation, during the growth process the impurities are stabilized at the surface of the growing nanoparticles by the dislocations resulting from the emerging extended lattice defects, being incorporated in the nanoparticles core during their further growth. The validity of this model of incorporation and the preferential localization of the Mn^{2+} ions in the core of the cZnS NPs was supported by the high resolution transmission electron microscopy observation of stacking faults and twins in more than 30 % of the investigated cZnS NPs. Moreover, the ELDA mechanism of incorporation can explain independent observations of high doping levels in small cZnS NPs grown at temperatures below 300 ºC, which could not be

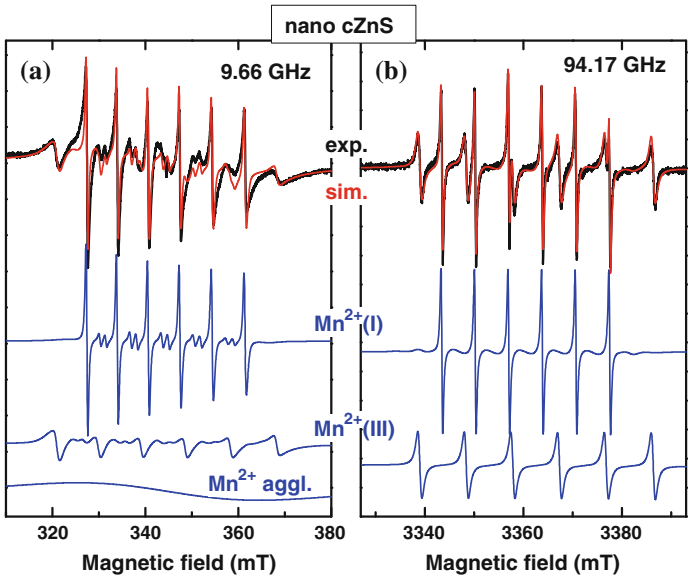

Fig. 1.5 Experimental (exp, *solid black line*) and simulated (sim, *red line*) EPR spectra of Mn^{2+} in small cZnS nanoparticles at low (X-band) and high (W-band) frequency. The simulated spectra are the sum of the calculated spectra of the individual centers displayed below

explained by the regular trapped-dopant based mechanism that requires larger, well faceted NPs [6, 38].

The Mn^{2+}(III) centers, also observed in the investigated cZnS:Mn^{2+} NPs (Fig. 1.5), exhibit SH parameters (Table 1.1) different from those of the Mn^{2+}(I) center and of the substitutional Mn^{2+} ions in the cZnS single crystal lattice [27]. Because no forbidden transitions could be observed for these centers due to the overlap with the more intense lines of the Mn^{2+}(I) centers, only a range of values could be determined for the B_2^0 parameter instead of an accurate value. The Mn^{2+}(III) centers were initially attributed to Mn^{2+} ions localized in a surface layer of the cZnS nanoparticles with neighboring H_2O molecules [30]. This structural identification was based on their thermal decomposition in air at T > 110 ºC, resulting in other Mn^{2+}(II) centers with smaller hyperfine splitting (Table 1.1). Later EPR investigations, using traces of substitutional Mn^{2+} ions as local paramagnetic probes, have shown that the crystalline ε-$Zn(OH)_2$ with orthorhombic symmetry decomposes in the same temperature range into nanocrystalline ZnO [22], as will be detailed in the next section. Considering the very close SH parameters (Table 1.1) of the Mn^{2+}(III) centers in cZnS NPs and of the substitutional Mn^{2+} ions in crystalline ε-$Zn(OH)_2$, it was proposed that the cZnS nanoparticles prepared at high pH values were covered by a shell of disordered ε-$Zn(OH)_2$ containing Mn^{2+} ions as Mn^{2+}(III) centers [39].

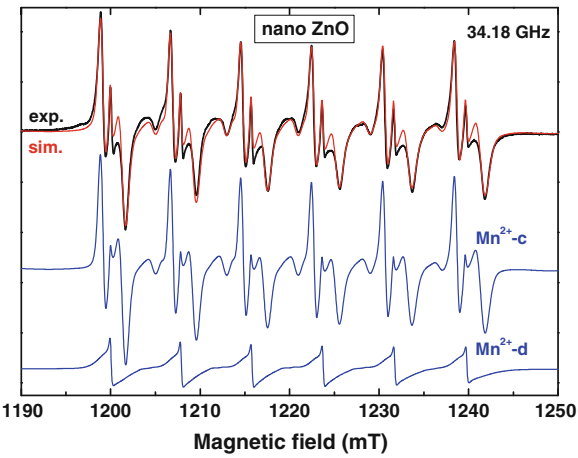

Fig. 1.6 The experimental (exp, *solid black line*) and simulated (sim, *red line*) Q-band EPR spectra of the Mn^{2+} ions in colloidal ZnO NPs. The simulated spectrum is the sum of the calculated spectra of the individual centers displayed below

1.2.3 Localization of the Mn^{2+} Ions in Colloidal ZnO Nanoparticles

The ZnO NPs investigated by EPR were prepared by adding 0.02 M [$Mn(CH_3–COO)_2.4H_2O$] to 15 ml of 0.19 M $Zn(NO_3)_2$ solution. The resulting solution was co-precipitated at pH = 9 with 10 ml 2.4 M NaOH and left for 2 h to mature at 50 ºC. In the post synthesis steps the precipitate was centrifuged, washed with bi-distilled water and absolute ethanol and dried for 6 h at 50 ºC. According to the XRD pattern from Fig. 1.4, the resulting material consisted of single wurtzite phase nanocrystalline ZnO with 30 nm average crystallites size.

The recorded EPR spectrum (Fig. 1.6) can be deconvoluted in two spectra, belonging to different Mn^{2+} centers present in the ZnO NPs. Their SH parameter values are very close to those of the Mn^{2+} in ZnO single crystals (Table 1.2), the main difference between the two centers being the different $\sigma(B_2^0)$ broadening parameter values. The two centers were identified as Mn^{2+} ions substituting the host lattice Zn^{2+} cations in the well crystallized ZnO NPs (the so-called Mn^{2+}-c centers,

Table 1.2 The SH parameters (*g*, *A*, *ZFS*) of the paramagnetic centers attributed to Mn^{2+} in nanostructured and single crystal ZnO

Lattice host/center	*g*	*A* (10^{-4} cm^{-1})	*ZFS* (10^{-4} cm^{-1})	ΔB_{pp} (mT)/ $\sigma(B_n^m)$ ($\%B_n^m$)	Reference
ZnO NPs /Mn^{2+}-c	2.0012	−74	$\|B_2^0\|$ = 80.1	0.15 (X, Q)/ 12.3 $\%B_2^0$	[21]
Disordered ZnO/Mn^{2+}-d	2.0012	−73.5	$\|B_2^0\|$ = 80.1	0.15 (X, Q)/ 43 $\%B_2^0$	[21]
ZnO single crystal / substitutional Mn^{2+}	2.0012	−73.4	$\|B_2^0\|$ = 75 $\|B_4^0\|$ = 0.0306	−/3$\%B_2^0$	[41]

The individual linewidth (ΔB_{pp}) for a specific microwave frequency band and the broadening parameter $\sigma(B_n^m)$ are also given

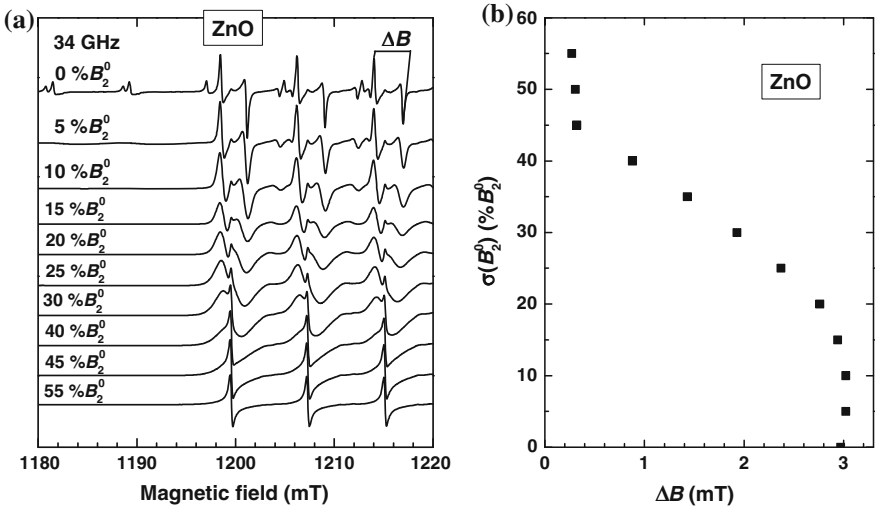

Fig. 1.7 **a** Simulated Q-band EPR spectra (partial view) of Mn^{2+} ions in nanocrystalline ZnO for different broadening parameter values. **b** The broadening parameter $\sigma(B_2^0)$ versus the powder linewidth ΔB for the $M_S : -1/2 \leftrightarrow +1/2$, M_I = -1/2 transition

with the smaller $\sigma(B_2^0)$) and Mn^{2+} ions localized in a small amount of disordered ZnO phase (the so-called Mn^{2+}-d centers, with the very large $\sigma(B_2^0)$) [21]. The smaller value of the hyperfine parameter of the Mn^{2+}-d centers compared to the Mn^{2+}-c centers was explained by the lower average coordination number of the Mn^{2+} ions [40] due to the disorder.

One can see in Fig. 1.6 that the difference in the broadening parameter value results in very different patterns for the simulated spectra of the Mn^{2+}-c and Mn^{2+}-d centers. The evolution of the simulated EPR spectra pattern of Mn^{2+} in ZnO with increasing broadening parameter (Fig. 1.7a) gives a helpful tip for the analysis and interpretation of the spectra [23]. For clarity reasons, in Fig. 1.7a only a portion of each spectrum, consisting of the three lower field lines from the central sextet and two non-central lines, was represented. According to the spectrum simulations the non-central lines disappear very fast, for broadening parameters of less than 10 % B_2^0. The central transitions are also strongly affected by the broadening. If we define the powder linewidth ΔB as the separation between the extreme (maximum and minimum) peaks corresponding to one of the central transitions (Fig. 1.7a), one can see that ΔB decreases as the broadening parameter increases (Fig. 1.7b). The variation is stronger for broadening parameters between 15 and 50 % B_2^0. For even larger broadening parameters the variation is insignificant. Still, the variation displayed in Fig. 1.7b allows one to evaluate the broadening parameter in the experimental spectrum of a ZnO:Mn^{2+} sample from a simple measurement of the separation between two points in the spectrum, without needing to perform a laborious simulation.

Another very important property was recently derived from the observation of the Mn^{2+} EPR spectra in ZnO nanoparticles prepared by different methods. Thus, Stefan et al. [23] observed that the broadening parameter of the Mn^{2+} spectra in the ZnO nanoparticles is correlated with the crystallite average size d, determined by XRD, according to an empirically determined exponential decay: $\sigma(B_2^0) \sim \exp(-d/\delta)$, where δ is a constant. This relationship does not depend on the preparation conditions of the ZnO nanoparticles, showing that the main contribution to the local strain in the nanoparticles is size related, or, more accurately, influenced by the surface to volume ratio. The relationship is assumed to be valid in the form given in the paper (with $\delta \sim 18$ nm) for ZnO nanoparticles which are not covered by a surface layer of another compound. The presence of such ligands on the nanoparticles surface could have an important ordering effect on the nanoparticles structure [5]. In case that such a layer exists, the relationship should still hold for larger nanoparticles (>20 nm), where the surface layer is not expected to affect the structural properties of the nanoparticles core. For smaller ZnO nanoparticles forming the core in a core/shell structure, the $\sigma(B_2^0) = f(d)$ relationship should be verified. As $\sigma(B_2^0)$ can be evaluated directly from the EPR spectrum, once the $\sigma(B_2^0) = f(d)$ relationship is established for a particular ZnO core/shell system, it follows that the ZnO nanoparticles average size can be determined from the powder linewidth of the Mn^{2+} EPR spectra.

As previously shown, EPR was used not only to determine the localization and ground state properties of the Mn^{2+} impurity ions in the semiconductor ZnS and ZnO nanoparticles, but also to observe and identify size related effects. Thus, in the case of cubic ZnS, for small (<3 nm) nanoparticles prepared at temperatures below 300 ºC, the doping with activating Mn^{2+} ions was found to take place through the ELDA mechanism rather than through the expected diffusion mechanism which needs larger NPs with well-defined facets. It is expected that this is a general property of the II–VI cubic semiconductor nanoparticles. However, it still needs to be tested for other host lattice/impurity ions systems.

In the case of the ZnO nanoparticles, a very important property is that the main contribution to the lattice disorder is size related, independent of the synthesis conditions of the nanoparticles. A survey of the recent literature shows that this seems to be a general feature of the nanoparticles, as a correlation between the EPR lines broadening parameter and the nanoparticle size has been also observed for other host lattice/impurity ions systems such as $PbTiO_3/Cr^{3+}$ [42], ZnO/Fe^{3+} [43] and LaF_3/Gd^{3+} [44].

It should be also noted that the observation of the Mn^{2+}(III) centers in cZnS nanoparticles and of the Mn^{2+}-d centers in nanostructured ZnO shows that indeed, as previously mentioned, it is possible to detect with EPR the presence of minute amounts of different compounds and to identify them even if they are in a disordered phase. Moreover, as will be further shown, it is possible to evidence the peculiar thermal decomposition behavior of the ε-$Zn(OH)_2$ as a nanostructured disordered shell covering the cZnS NPs, different from the bulk compound.

1.3 Probing Structural/Chemical Transformations in (Nano)Crystalline Materials with EPR of Low Concentration Levels of Mn^{2+} Impurities

EPR spectroscopy using low concentrations of Mn^{2+} ions as local paramagnetic probes can offer a wealth of information about the thermally induced chemical and/or structural transformation of the host nanomaterials. Such investigations are based on the pulse annealing EPR experiments [45]. In these experiments the investigated samples are pulse annealed for short equal periods of time at temperatures which are increased in constant steps. After each annealing step the sample is cooled down to the measuring temperature (RT, or even a lower one where the observed Mn^{2+} centers are thermally stable) and its EPR spectrum is recorded. By such a procedure, firstly employed for investigating the transformation kinetics of the color centers in alkali halides [46–48], one obtains a set of EPR spectra reflecting in a 'frozen sequence" the temperature induced transformations (production and decay) of the paramagnetic centers contained in the investigated sample and further on, one obtains information about the composition and/or structure of the surrounding nanomaterial.

1.3.1 Thermal Decomposition of Zn Based Compounds into Nanostructured ZnO Probed with EPR

ZnO is an attractive material for a broad range of applications and there is an important amount of research dedicated to finding more efficient methods for producing functionalized nanoparticles with controlled size, morphology and, especially, doped with controlled amounts of TMIs. A promising method for obtaining ZnO nanoparticles with controlled doping levels consists in the thermal decomposition of Zn based compounds which can be more easily doped with TMIs [49–51]. However, the thermally induced transformation of these compounds into ZnO and the further growth of the ZnO nanoparticles should be carefully monitored in order to establish the optimal conditions for obtaining ZnO nanoparticles with the required structural properties.

EPR was recently used to obtain detailed information about the structural changes taking place in two Zn-based precursor compounds during thermo-chemical treatments and to monitor their decomposition into nanostructured ZnO [21, 22].

One of the investigated precursors was crystalline ε-$Zn(OH)_2$ with orthorhombic structure prepared by liquid-liquid reaction, containing trace amounts (<0.1 ppm) of unintentional Mn^{2+} impurity ions. From EPR pulse annealing experiments in air it was determined that ε-$Zn(OH)_2$ decomposes into ZnO nanoparticles in the 110–140 ºC temperature range [22]. Figure 1.8 displays the EPR spectra measured at three different moments of the ε-$Zn(OH)_2$ to ZnO thermally induced transformation. They correspond to the starting, as grown (AG) crystalline ε-$Zn(OH)_2$, the

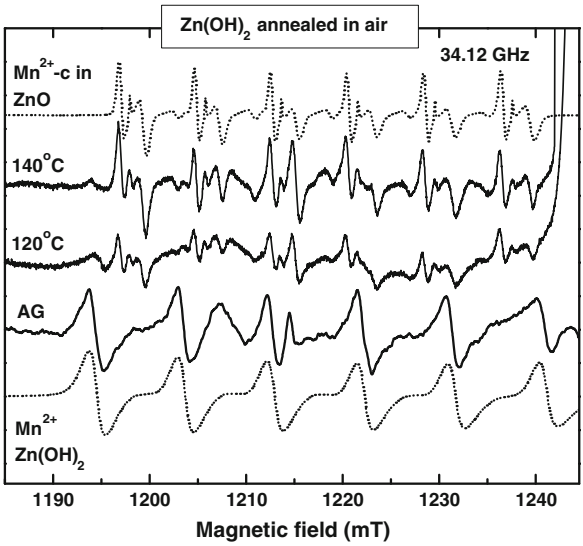

Fig. 1.8 Thermally induced decomposition/transformation of ε-$Zn(OH)_2$ into nanostructured ZnO, as shown by changes in the Q-band EPR spectra at RT of probing substitutional Mn^{2+} ions. The simulated EPR spectra (*dot lines*) of the Mn^{2+} ions in the ε-$Zn(OH)_2$ and ZnO pure phases are also included

coexistence of the ε-$Zn(OH)_2$ and ZnO phases at an intermediate temperature (T_{ann} = 120 ºC) in the transformation range and the resulting ZnO nanocrystallites of 53 nm average diameter, as determined from XRD measurements (T_{ann} = 140 ºC). The simulations of the EPR spectra of the Mn^{2+} ions in the ε-$Zn(OH)_2$ and ZnO pure phases are also provided, in order to help in the identification of the two compounds. In this investigation the Mn^{2+} ions are used as local atomic probes, their EPR spectra reflecting the temperature induced changes in the structure and/or composition of the host lattice.

The other investigated precursor of the nanostructured ZnO consisted of commercial grade hydrozincite (abbreviated ZCB), or zinc carbonate basic $[Zn_5(CO_3)_2(OH)_6]$, from Alfa Aesar, which was found to transform into ZnO by thermal decomposition in the temperature ranges of 225–255 ºC in air and 175–235 ºC in vacuum, respectively [21]. The starting material contained less than 200 ppm of unintentional Mn^{2+} impurities, localized as the substitutional centers Mn^{2+}(A) and Mn^{2+}(B) in octahedrally and tetrahedrally coordinated Zn^{2+} sites, respectively, of ZCB. As in the case of ε-$Zn(OH)_2$, three EPR spectra are displayed in Fig. 1.9, measured before (AG), during (245 ºC) and after the transformation (275 ºC), as well as the simulations of the EPR spectra of the Mn^{2+} ions in the ZCB and ZnO pure phases. In this case the resulting nanostructured ZnO consisted of a mixture of disordered phase and crystalline nanoparticles, containing the corresponding (Mn^{2+}-d) and (Mn^{2+}-c) centers. The formation of the nanostructured ZnO was found to be a two steps process, in which the disordered ZnO, initially produced by the thermal decomposition of ZCB, further transforms into nanocrystalline ZnO.

The nanoparticles were found to be consistently smaller at the same annealing temperature for the sample annealed in vacuum compared to the sample annealed in air. The formation of a disordered nanostructured ZnO in the first stage of the

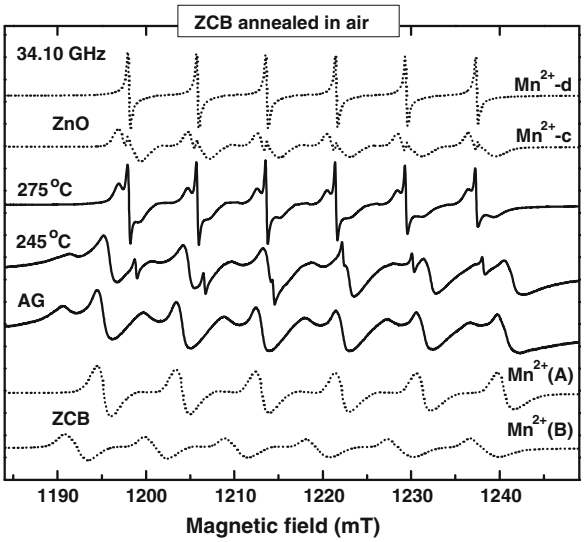

Fig. 1.9 Thermally induced decomposition /transformation of ZCB into nanostructured ZnO reflected in changes in the Q-band EPR spectra at RT of probing substitutional Mn^{2+} ions during a pulse annealing experiment. The simulated EPR spectra (dot lines) of the Mn^{2+} ions in the ZCB and ZnO pure phases are also included (Based on Fig. 1.4a from [21]. Reprinted with permission from Cryst. Growth Des. **11**, 5030 (2011). Copyright 2011 American Chemical Society.)

thermal decomposition of the ZCB has been attributed to the violent expulsion of the CO_2 and H_2O gases, which breaks the ZCB crystal lattice bonds. The eruptive-like thermal decomposition process of nanocrystalline ZCB could be slowed down and directly observed in a transmission electron microscope, in which the ZCB target was cooled down with liquid nitrogen and locally heated by the microscope electron beam [52].

Changes in the composition and structure of the precursor material and the resulting nanostructured ZnO could be observed in the EPR spectra of both ε-$Zn(OH)_2$ and ZCB precursors. The thermo-chemical conditions of the structural/chemical transformations were accurately established for both compounds, which is very important for the synthesis of ZnO nanoparticles with controlled size and size distribution. The SH parameters determined from the EPR spectra of the substitutional Mn^{2+} ions in the two precursors will further serve as reference data for the identification of these compounds in other systems, as they tend to be formed quite often as a result of corrosion/interaction of the nanostructured ZnS or ZnO with the surrounding atmosphere. Moreover, the presence of the substitutional Mn^{2+} impurity ions in comparable concentrations in the precursors and resulting nanostructured ZnO demonstrates that doping the precursors with required amounts of activating impurities and transforming them in nanosized ZnO can be a workable possibility to obtain nanosized ZnO with a high impurity ions content, ions which are otherwise strongly segregated during the direct synthesis.

1.3.2 The Mechanism of ZnO Nanocrystallization Determined by EPR

In order to prepare ZnO nanoparticles with controlled size and size distribution, it is important to know the optimum growth conditions, and therefore the growth mechanism. Detailed information about the nanocrystallization process of the ZnO resulting from the thermal decomposition in air of ZCB was acquired by EPR, using the empirical relationship determined between the line broadening parameter $\sigma(B_2^0)$ and the average crystallite size d of the nanoparticles [23]. From the isothermal variation of d versus the annealing duration at several temperatures it was concluded that, at lower temperatures (<400 ºC), the nanoparticles growth took place by a structural relaxation mechanism [53], consisting in the rearrangement of the atoms at interfaces, driven by the reduction of the surface induced strain. The activation energy for this process was determined to be 23 kJ/mol. At higher temperatures the atom diffusion at interfaces became active as well, with activation energy of 79 kJ/mol. This signals a change in the growth mechanism at higher temperatures and for longer annealing durations, from structural relaxation to diffusion based growth.

Additional information was obtained by using the ability of EPR to observe and distinguish both the disordered and nanocrystalline phases of ZnO [23]. By double integration of the EPR spectrum of a Mn^{2+} center one can obtain the concentration of the respective center in a sample. As the Mn^{2+}-d and Mn^{2+}-c centers are uniformly distributed in the total ZnO volume, the evolution of their concentrations during various thermal treatments reflects the evolution of the corresponding ZnO phases. The relative concentration of the Mn^{2+}-c centers, f_c, is thus proportional with the crystallized fraction of ZnO (ZnO nanoparticles) from the total ZnO volume.

Figure 1.10 displays the evolution of f_c versus the average crystallite size d for samples submitted to different thermal treatments, namely pulse annealing at various temperatures for equal durations and isothermal annealing at 300, 400 and 500 ºC, respectively, for different durations. As one can see in the figure, the nanoparticles growth process takes place in two stages, independent of the annealing algorithm. During the first stage the crystallized fraction grows sharply with the size increase, until it reaches a value of about 75 % of the total ZnO at temperatures of less than 400 ºC. This stage corresponds to the low temperature growth by structural relaxation. From Fig. 1.10 it is obvious that for nanoparticles isothermally annealed at 300 ºC only the first growth stage is active, while for the pulse annealed sample the contribution of the second stage begins at an annealing temperature larger than 350 ºC. For the samples isothermally annealed at 400 ºC and 500 ºC the second growth stage is active from the beginning of the treatment.

The second stage is characterized by a very small variation in the crystallized fraction for a considerable increase of the crystallites size. The larger nanoparticles seem to grow at the expense of the smaller ones, a process driven by the reduction of the total grain boundary energy. Indeed, the evolution of the intercrystalline

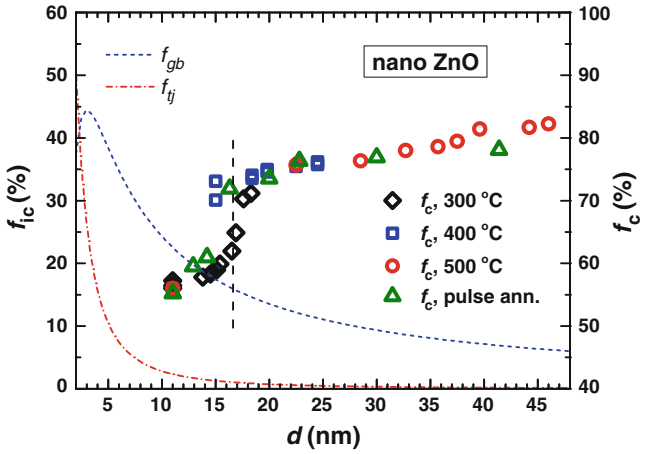

Fig. 1.10 The experimental volume fraction of the ZnO nanoparticles (f_c) and the calculated volume fractions of the intercrystalline components ($f_{gb} + f_{tj} = f_{ic}$) versus the average crystallite size (Based on Fig. 1.9 from [23]. Reprinted with permission from Cryst. Growth Des. **13**, 1350 (2013). Copyright 2013 American Chemical Society.)

region f_{ic}, assumed to consist of the grain boundaries between two nanoparticles and the triple junctions at the contact of three nanoparticles, supports this mechanism. In Fig. 1.10 the evolution of the intercrystalline component volume fractions with the average crystallite size d of the nanoparticles takes place according to the relationships [54]:

$$\begin{aligned} f_{ic} &= 1 - \frac{(d-\Delta)^3}{d^3} \\ f_{gb} &= 1 - \frac{3\Delta(d-\Delta)^2}{d^3} \\ f_{tj} &= f_{ic} - f_{gb} \end{aligned} \tag{1.8}$$

Here Δ is the grain boundary width with a generally accepted value of 1 nm. One can see that at the onset of the second stage the triple junction fraction f_{tj} is almost zero and the grain boundary fraction f_{gb} decreases to a third of its maximum value. The nanoparticles are in an increased contact which facilitates the transfer of atoms from the smaller ones to the larger ones.

It is clear from these results that a considerable growth can be achieved for the ZnO nanoparticles by annealing at quite low temperatures (up to 300 ºC) [21], therefore without risking phase segregation or the formation of new compounds, which could affect the intended properties. Also, at these temperatures where the first growth regime is active, a narrower size distribution is expected, while at higher temperatures, where the diffusion is activated and the larger nanoparticles grow at the expense of the smaller ones, the size distribution is expected to broaden

considerably. Previous TEM investigations confirm this result. Thus, it was found that the ZnO sample pulse annealed in air up to 300 ºC consists of nanoparticles of 8–15 nm in size [21], while in the sample annealed up to 625 ºC the size range is from 15 to 85 nm. These results can be used to fine-tune the synthesis conditions by changing the annealing temperature, duration and atmosphere composition in order to obtain ZnO nanoparticles with controlled average size and size distribution.

1.3.3 The Thermal Decomposition of the ε-Zn(OH)$_2$ Shell of cZnS NPs with a Core-Shell Structure

The thermal decomposition of the ε-Zn(OH)$_2$ shell of the cZnS NPs with a core-shell structure, reflected in the decay of the Mn^{2+}(III) centers into Mn^{2+}(II) centers, as mentioned in Sect. 1.2.2, lead to a puzzling result. Namely, the SH parameters of the Mn^{2+}(II) centers, expected to consist of substitutional Mn^{2+} ions localized in a disordered ZnO shell, did not correspond to the expected SH parameters. Indeed, the hf splitting parameter $A = -80.5 \times 10^{-4}$ cm^{-1} for the Mn^{2+}(II) surface centers (Table 1.1) is much larger compared to the expected $A = -74 \times 10^{-4}$ cm^{-1} parameter for the Mn^{2+} ions in nanocrystalline ZnO (Table 1.2). The answer to this puzzling result was found from a recent detailed investigation by pulse annealing EPR experiments on cZnS NPs with and without a ε-Zn(OH)$_2$ shell, doped with low concentrations of Mn^{2+} ions [24]. From the analysis of the resulting data it was concluded that the thermal decomposition in air of the nanosized, disordered ε-Zn(OH)$_2$ shell is different from the one step thermal decomposition around 120 ºC of the bulk crystalline ε-Zn(OH)$_2$. Thus, it was found that the thermal decomposition of the ε-Zn(OH)$_2$ nanosized shell into nanocrystalline ZnO is a three steps process, which takes place over the 80–450 ºC temperature range. It also involves the formation of two new zinc oxyhydrate compounds, $Zn_2O(OH)_2$ and $Zn_4O_3(OH)_2$, at the intermediate temperatures of above 80 ºC and 250 ºC, respectively, in air, which have not been observed in bulk crystalline state so far. In such circumstances, the decay of the Mn^{2+}(III) into Mn^{2+}(II) centers corresponds to the partial dehydration of only two of the four nearest neighboring pairs of hydroxyl groups tetrahedrally coordinating the substitutional Mn^{2+} cation in the ε-Zn(OH)$_2$ shell.

1.4 Conclusions

We have shown in this chapter how EPR can be used to both determine the localization of the Mn^{2+} ions present in low concentrations in Zn based semiconductor nanoparticles and gather information about the structural properties of the host lattice using the paramagnetic impurity as an atomic probe. With proper adjustments of the EPR experiments and accurate numerical analysis of the

resulting spectra it was possible to obtain accurate SH parameters for the various Mn^{2+} centers involved which, further on, provided a wealth of information about the local structure, as well as the structural and chemical transformations of the host nanoparticles.

The size specific properties, which we have evidenced, have important repercussions for the envisaged applications of the semiconductor nanoparticles. The presence of a local axial crystal field acting on the core localized Mn^{2+} activating ions should be taken into consideration when evaluating the optical properties of the nanoparticles, of interest in many technological applications. Thus, the associated changes in the local crystal field symmetry and intensity are expected to affect the resulting optical spectra [55, 56]. The extended lattice defect assisted incorporation of impurities in small cubic ZnS nanoparticles affects the final concentration of Mn^{2+} impurities in the nanoparticles core. At higher concentration levels the predominant localization of the impurities near the extended defects could be favorable for their aggregation in specific lattice planes of cZnS parallel to the extended defects, with consequences for the magnetic properties. The proposed extended lattice defects assisted (ELDA) mechanism of incorporation seems to be also active in the first stage growth of other cubic II–VI nanocrystals. This is a subject which remains to be investigated. The observed correlation between the lattice disorder and the average crystallite size of the ZnO nanoparticles is important for material properties related to optical and electronic processes.

Probing the structural and chemical changes undergone by the Zn-based compounds has also a considerable application interest, as it allows the fine tuning of the synthesis algorithms in order to obtain semiconductor nanoparticles with controlled doping levels, size, size distribution and structure. As demonstrated by our examples, EPR is a worthy tool in this endeavor, as it provides a ready feedback not only about the localization of the dopants, but also about the structure, particle size and phases present in the nanostructures resulted from a specific thermo-chemical treatment, with an accuracy level that is not always available with other regularly employed structural methods, such as XRD or TEM.

Acknowledgments The original work described here was supported by CNCSIS-UEFISCSU through projects no. 788/2006, CEX no. 38/2006, PN-II-ID-PCE no. 523/2008 and PN-II-ID no.74/2011. We would like to thank Leona C. Nistor, Doina C. Mateescu, Narcis J. Barascu, Ioana Vlaicu and Dan Zernescu for contributions along the years to the work contained within the manuscript. This chapter was written through equal contributions of all authors.

References

1. A.P. Alivisatos, J. Phys. Chem. **100**, 13226 (1996)
2. D. Bera, L. Quian, T.K. Tseng, P.H. Holloway, Materials **3**, 2260 (2010)
3. R. Beaulac, S.T. Ochsenbein, D.R. Gamelin, *Colloidal Transition-Metal Doped Quantum Dots*, ed. by V.I. Klimov Nanocrystals quantum dots, 2nd edn. (CRC Press, New York, 2010)
4. F. Huang, B. Gilbert, H. Zhang, J.F. Banfield, Phys. Rev. Lett. **92**, 155501 (2004)

5. B. Gilbert, F. Huang, L. Zhang, C. Goodell, H. Zhang, J.F. Banfield, Nano Lett. **6**, 605 (2006)
6. D.J. Norris, A.L. Efros, S.C. Erwin, Science **319**, 1776 (2008)
7. R. Buonsanti, D.J. Miliron, Chem. Mater. **25**, 1305 (2013)
8. H. Hu, W. Zhang, Opt. Mater. **28**, 536 (2006)
9. X.S. Fang, T.Y. Zhai, U.K. Gautam, L.A. Li, L.M. Wu, B. Yoshio, D. Golberg, Prog. Mater Sci. **56**, 175 (2011)
10. X.S. Fang, Y. Bando, U.K. Gautmam, T.Y. Zhai, H. Zong, X. Xu, M.Y. Liao, D. Goldberg, Crt. Rev. Sol. St. Mat. Sci. **34**, 190 (2009)
11. K. Manzoor, S. Johny, D. Thomas, S. Seuta, D. Menon, S. Nair, Nanotechnology **20**, 065102 (2009)
12. R.E. Anderson, W.C.W. Chan, ACS Nano **7**, 1301 (2008)
13. R. Beaulac, P.I. Archer, D.R. Gamelin, J. Sol. St. Chem. **181**, 1582 (2008)
14. R. Beaulac, P.I. Archer, S.T. Ochsenbein, D.R. Gamelin, Adv. Funct. Mater. **18**, 3873 (2008)
15. R. Beaulac, Y. Feng, J.W. May, E. Badaeva, D.R. Gamelin, X. Li, Phys. Rev. B **84**, 195324 (2011)
16. A. Abragam, B. Bleaney, *Electron Paramagnetic Resonance of Transition Ions* (Clarendon Press, Oxford, 1970)
17. J.R. Pilbrow, *Transition Ion Electron Paramagnetic Resonance* (Clarendon Press, Oxford, 1990)
18. S. Bhattacharyya, D. Zitoun, A. Gedanken, Nanosci. Nanotech. Lett. **3**, 541 (2011)
19. D. Ghica, S.V. Nistor, L.C. Nistor, M. Stefan, C.D. Mateescu, J. Nanopart. Res. **13**, 4325 (2011)
20. S.V. Nistor, D. Ghica, L.C. Nistor, M. Stefan, C.D. Mateescu, J. Nanosci. Nanotechnol. **11**, 9296 (2011)
21. S.V. Nistor, L.C. Nistor, M. Stefan, D. Ghica, Gh Aldica, J.N. Barascu, Cryst. Growth Des. **11**, 5030 (2011)
22. S.V. Nistor, D. Ghica, M. Stefan, I. Vlaicu, N.J. Barascu, C. Bartha, J. Alloys Comp. **548**, 222 (2013)
23. M. Stefan, S.V. Nistor, D. Ghica, Cryst. Growth Des. **13**, 1350 (2013)
24. S.V. Nistor, D. Ghica, M. Stefan, L.C. Nistor, J. Phys. Chem. C **117**, 22017 (2013)
25. M. Stefan, S.V. Nistor, N.J. Barascu, J. Magn. Reson. **210**, 200 (2011)
26. C. Rudowicz, Magn. Res. Rev. **13**, 1 (1987)
27. S.V. Nistor, M. Stefan, J. Phys.: Condens. Matter **21**, 145408 (2009)
28. S.V. Nistor, L.C. Nistor, M. Stefan, C.D. Mateescu, R. Birjega, N. Solovieva, M. Nikl, Superlattices Microstruct. **46**, 306 (2009)
29. S.V. Nistor, M. Stefan, L.C. Nistor, E. Goovaerts, G. Van Tendeloo, Phys. Rev. B **81**, 035366 (2010)
30. M. Stefan, S.V. Nistor, D. Ghica, C.D. Mateescu, M. Nikl, R. Kucherkova, Phys. Rev. B **83**, 045301 (2011)
31. R.S. Title, *Paramagnetic Resonance Studies*, In *Physics and Chemistry of II-VI Compounds*, ed. by M. Aven, J.S. Prener, (North-Holland Publishing Company, Amsterdam, 1967)
32. S. Stoll, A. Schweiger, J. Magn. Reson. **178**, 42 (2006)
33. J. Kliava, Phys. Stat. Sol. (b) **134**, 411 (1986)
34. L.C. Nistor, C.D. Mateescu, R. Birjega, S.V. Nistor, Appl. Phys. A **92**, 295 (2008)
35. A. Ya. Yakunin, I.V. Shtambar, A.S. Kushnir, S.A. Omelchenko, Russ. Phys. J. **16**, 1375 (1973)
36. T. Buch, B. Clerjaud, B. Lambert, P. Kovacs, Phys. Rev. B **7**, 184 (1973)
37. S.V. Nistor, M. Stefan, L.C. Nistor, D. Ghica, C.D. Mateescu, N.J. Barascu, IOP Conf. Series: Mat. Sci. Eng. **15**, 012024 (2010)
38. M.H. Du, S.C. Erwin, Al. L. Efros, Nanolett. **8**, 2878 (2008)
39. S.V. Nistor, M. Stefan, D. Ghica, L.C. Nistor, Rad. Meas. **56**, 40 (2013)
40. E. Simanek, K.A. Muller, J. Phys. Chem. Sol. **31**, 1027 (1970)
41. M. Diaconu, H. Schmidt, A. Poppl, R. Bottcher, J. Hoentsch, A. Klunker, D. Spemann, H. Hochmuth, M. Lorenz, M. Grundmann, Phys. Rev. B **72**, 085214 (2005)

42. E. Erdem, R. Bottcher, H.J. Glasel, E. Hartmann, Magn. Reson. Chem. **43**, S174 (2005)
43. M. Açıkgöz, M.D. Drahus, A. Ozarowski, J. van Tol, S. Weber, E. Erdem, J. Phys.: Condens. Matter **26**, 155803 (2014)
44. A.M. Gazizulina, E.M. Alakshin, E.I. Baibekov, R.R. Gazizulin, MYu. Zakharov, A.V. Klochkov, S.L. Korableva, M.S. Tagirov, JETP Lett. **99**, 149 (2014)
45. S.V. Nistor, M. Stefan, D. Ghica, J. Therm. Anal. Calorim. (2014). doi:10.1007/s10973-014-3743-1
46. C.J. Delbecq, D. Schoemaker, P.H. Yuster, Phys. Rev. B **3**, 473 (1971)
47. S.V. Nistor, E. Goovaerts, B.R. Yang, D. Schoemaker, Phys. Rev. B **28**, 1219 (1983)
48. S.V. Nistor, I. Heyndrickx, E. Goovaerts, A. Bouwen, D. Schoemaker, Phys. Stat. Sol. (b) **130**, 175 (1985)
49. V. Ischenko, S. Polarz, D. Grote, V. Stavrache, K. Fink, M. Driess, Adv. Funct. Mat. **15**, 1945 (2003)
50. S. Wang, G. Xia, J, Shao , Z. Fan, J. Alloys Compd. **424**, 304 (2006)
51. Z. Mickovic, D.T.L. Alexander, A. Sienkiewicz, M. Mionic, L. Forro, A. Magrez, Cryst. Growth Des. **10**, 4437 (2010)
52. L.C. Nistor, S.V. Nistor, D. Ghica, Rom. Rept. Phys. **65**, 186 (2013)
53. C.H. Shek, J.K.L. Lai, G.M. Lin, Nanostruct. Mater. **11**, 887 (1999)
54. G. Palumbo, S.J. Thorpe, K.T. Aust, Scr. Metall. Mater. **24**, 1347 (1990)
55. N.K. Datta, S. Pal, M. Ghosh, Chem. Phys. **400**, 44 (2012)
56. S. Pal, M. Ghosh, Superlat. Microstruct. **55**, 118 (2013)

http://www.springer.com/978-3-662-44478-8

Size Effects in Nanostructures
Basics and Applications
Kuncser, V.; Miu, L. (Eds.)
2014, XVI, 325 p. 163 illus., 45 illus. in color., Hardcover
ISBN: 978-3-662-44478-8